

Cohesive modeling of dynamic fracture in functionally graded materials

SOMA SEKHAR V. KANDULA^{1,*}, JORGE ABANTO-BUENO², PHILIPPE H. GEUBELLE and JOHN LAMBROS¹

¹*Department of Aerospace Engineering, University of Illinois at Urbana-Champaign, 306 Talbot Lab, Urbana, IL 61801, USA*

**Author for correspondence (E-mail: geubelle@uiuc.edu)*

²*Department of Mechanical Engineering, Bradley University, 1501 West Bradley Avenue, Peoria, IL 61625, USA*

Received 8 April 2004; accepted in revised form 25 January 2005

Abstract. The dynamic fracture of functionally graded materials (FGMs) is modeled using an explicit cohesive volumetric finite element scheme that incorporates spatially varying constitutive and failure properties. The cohesive element response is described by a rate-independent bilinear cohesive failure model between the cohesive traction acting along the cohesive zone and the associated crack opening displacement. A detailed convergence analysis is conducted to quantify the effect of the material gradient on the ability of the numerical scheme to capture elastodynamic wave propagation. To validate the numerical scheme, we simulate dynamic fracture experiments performed on model FGM compact tension specimens made of a polyester resin with varying amounts of plasticizer. The cohesive finite element scheme is then used in a parametric study of mode I dynamic failure of a Ti/TiB FGM, with special emphasis on the effect of the material gradient on the initiation, propagation and arrest of the crack.

Key words: Cohesive modeling, dynamic fracture, fracture toughness, functionally graded materials, wave propagation.

1. Introduction

Since their introduction by Kawasaki and Watanabe (1987) in high temperature metal/ceramic aerospace components, functionally graded materials (FGMs) have found a wide range of commercial applications including cutting tools, biomedical devices, optical fibers, optical filters and wear resistant coatings (Uemura, 2003). In many of these applications, FGMs provide an attractive way for the designer to tailor the microstructure to specific operating conditions, while minimizing the difficulties associated with discrete material interfaces. Very often, however, fracture resistance constitutes the primary design criterion, and this fact has led to the development of a special branch of fracture mechanics devoted to the failure of this class of materials.

Because of the complexity associated with spatially varying constitutive and failure properties, purely analytical treatments of such fracture problems have been limited to simple geometrical settings and loading conditions. Eischen (1987) analytically showed that the asymptotic stress field at the crack tip in a continuous and differentiable FGM is identical to that of a homogeneous material and the square

root singularity is preserved. A similar conclusion was reached by Jin and Noda (1994) for a piecewise differentiable FGM. Some of the early theoretical investigations involving quasi-static cracks in FGMs, concentrated on determination of the stress intensity factors (Erdogan, 1995), crack deflections (Gu and Asaro, 1997) and fracture resistance curves (Jin and Batra, 1996). The mode I fracture problem of a crack parallel to the gradient direction has been analyzed by Choi (1996). The first attempt of solving the steady state crack propagation in a FGM with exponentially varying moduli was made by Atkinson and List (1978). Stress and displacement fields around a dynamic crack moving at steady state in a FGM were determined by Parameswaran and Shukla (1999, 2002). The mathematical complexity is especially high in the dynamic case, and some of the analytical solutions available to date involve stationary mode III (Babaei and Lukasiewicz, 1998) and penny shaped (Li et al., 1999; Wang et al., 1999; Feng and Zou, 2003) cracks, steady state propagating cracks under in-plane (Jiang and Wang, 2002; Meguid et al., 2002) and normal (Meguid et al., 2002; Lee, 2004) loadings.

On the experimental side, the difficulty and cost of manufacturing large size fracture specimens amenable to testing has led most investigators to develop model FGMs. Lambros et al. (1999) have used an UV-sensitive material whose stiffness and fracture toughness depend strongly on the amount of UV exposure. Butcher et al. (1999) used a gravity casting technique to manufacture a particulate epoxy composite with spatially varying reinforcement concentration. Parameswaran and Shukla (1998), in a publication used in the present paper as the basis for a validation exercise, created a polyester-based FGM by controlling the plasticizer content. Chalivendra et al. (2003) fabricated a graded polyester composite with varying content of cenospheres using a buoyancy assisted casting process.

Several experimental techniques were developed to characterize these model FGMs. Li et al. (2000) and Abanto-Bueno and Lambros (2002) extracted the stress intensity factor values for FGM fracture specimens made of the UV-sensitive material using a hybrid experimental/numerical technique and full-field digital image correlation. Rousseau and Tippur (2001) used coherent gradient sensing and obtained the stress intensity factors using the quasi-static asymptotic expressions developed by Eischen (1987) and the dynamic ones obtained by Parameswaran and Shukla (1999). The crack growth and dynamic stress intensity factor history for their model FGMs were determined using photoelasticity by Parameswaran and Shukla (1998).

The difficulty in performing these type of experiments has led many analysts to adopt numerical schemes and solve FGM-related fracture problems. Although boundary integral formulations have been used in some cases (Yue et al., 2003; Zhang et al., 2003), the finite element (FE) method is by far the approach most commonly adopted. Batra (1980), Santare and Lambros (2000) and Paulino and Kim (2002) have incorporated the material property variation within the FE formulation. Santare et al. (2003) extended the graded FE concept to dynamic events and numerically modeled one-dimensional wave propagation in FGMs, comparing their results with the analytical solution of Chiu and Erdogan (1999). One-dimensional wave propagation in FGMs was also studied by Banks-Sills et al. (2002). Recently, Wang and Nakamura (2004) reviewed some of the existing models for crack growth simulations and chose a cohesive methodology to simulate dynamic crack propagation in

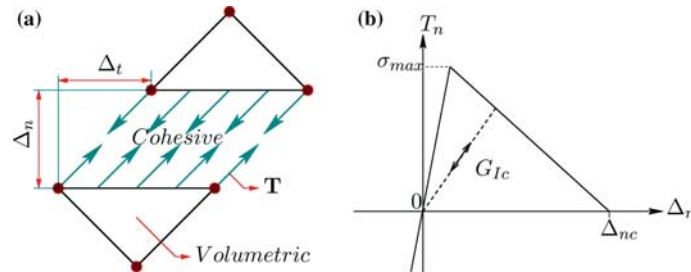


Figure 1. (a) Schematic of the CVFE concept, showing how a cohesive element is introduced between two volumetric elements. The cohesive element is shown in its deformed state: originally it has no thickness and the adjacent nodes are superposed. (b) Schematic of the bilinear cohesive model for mode I. The dashed line shows potential unloading and reloading paths.

elastic–plastic FGMs. Cohesive modeling was also used by Jin et al. (2002, 2003) to simulate quasi-static crack propagation in FGMs.

We summarize hereafter a detailed numerical study of dynamic fracture in FGMs using a simple cohesive failure model implemented in an explicit finite element scheme referred to as the Cohesive–Volumetric Finite Element (CVFE) scheme. Beyond the description and implementation of the cohesive model summarized in Section 2, the present paper focuses on the following three aspects: in Section 3, we show how the material gradient can affect the precision of the FE scheme in capturing elastodynamic wave propagation. In Section 4, we validate the CVFE scheme through comparison with experimental observations made in Parameswaran and Shukla (1998) during the dynamic failure of model polyester-based FGM specimens. Finally, we perform in Section 5 a detailed parametric study of mode I dynamic fracture of a Titanium Monoboride (TiB)/Titanium (Ti) FGM. This particular material is chosen because of its potential as protective coating in armor applications (Gooch et al., 1999).

2. Numerical method

As indicated earlier, the numerical method used in this analysis is the CVFE scheme that has been shown to be quite successful in the simulation of a variety of dynamic fracture events (Camacho and Ortiz, 1996; Xu and Needleman, 1996; Espinosa et al., 1998; Geubelle and Baylor, 1998; Bi et al., 2002; Maiti and Geubelle, 2004). This scheme relies on a combination of volumetric elements used to describe the constitutive response of the material and cohesive elements introduced to model the failure process. As shown schematically in Figure 1(a), the cohesive elements are placed along the edges of the volumetric elements and are characterized by a cohesive failure relation between the cohesive traction vector $\mathbf{T} = \langle T_n, T_t \rangle$ and the displacement jump vector $\mathbf{\Delta} = \langle \Delta_n, \Delta_t \rangle$, where the subscripts ‘*n*’ and ‘*t*’, respectively, denote the normal and tangential components (Figure 1b).

The present study focuses on the dynamic propagation of mode I cracks in the direction parallel to the material gradient and in the absence of branching. The cohesive elements are thus placed along the plane of the pre-existing crack and the cohesive model is characterized only by the relation between the normal components T_n

and Δ_n . We adopt hereafter the simple bilinear relation

$$T_n = \frac{\mathcal{S}}{1 - \mathcal{S}} \frac{\sigma_{\max}}{\mathcal{S}_{\text{initial}}} \frac{\Delta_n}{\Delta_{nc}},$$

where σ_{\max} and Δ_{nc} , respectively denote the local values of the tensile failure strength and critical crack opening displacement of the material Figure 1(b). The damage parameter \mathcal{S} is defined by

$$\mathcal{S} = \left\langle 1 - \frac{\Delta_n}{\Delta_{nc}} \right\rangle,$$

where $\langle z \rangle = z$ if $z > 0$ and $= 0$ otherwise. To prevent healing of the cohesive zone in the event of unloading, \mathcal{S} is constrained to be monotonically decreasing from its initial value $\mathcal{S}_{\text{initial}}$ chosen close to unity (typically 0.98 in this analysis) to its final value of zero, at which point complete failure is assumed. The area under the cohesive failure curve corresponds to the mode I fracture toughness G_{Ic} , which, in the present bilinear model, is given by

$$G_{Ic} = \frac{1}{2} \Delta_{nc} \sigma_{\max}. \quad (1)$$

To account for the possible appearance of large rotations during the fracture event, we use a nonlinear kinematic description of the motion. Denoting the location of a material point by \mathbf{x} in the initial undeformed configuration and $\bar{\mathbf{x}}$ in the deformed configuration at time t , the displacement \mathbf{u} , deformation gradient tensor \mathbf{F} and Lagrangian strain tensor \mathbf{E} are given by

$$\mathbf{u} = \bar{\mathbf{x}} - \mathbf{x}, \quad \mathbf{F} = \frac{\partial \bar{\mathbf{x}}}{\partial \mathbf{x}}, \quad \mathbf{E} = \frac{1}{2} (\mathbf{F}^T \mathbf{F} - \mathbf{I}),$$

where \mathbf{I} is the identity tensor.

Since the strains are expected to be small, we adopt the linear constitutive relation

$$\mathbf{S} = \mathbf{L}\mathbf{E},$$

where \mathbf{L} is the fourth-order tensor representing the isotropic elastic properties of the FGM and \mathbf{S} is the second Piola–Kirchhoff stress tensor related to the Cauchy stress tensor σ by

$$\sigma = \frac{1}{J} \mathbf{F} \mathbf{S} \mathbf{F}^T,$$

with J denoting the determinant of deformation gradient.

The numerical implementation of the CVFE scheme is similar to that used by Geubelle and Baylor (1998) and Bi et al. (2002). It relies on an explicit central difference time stepping scheme to update the nodal displacements, velocities and accelerations. The spatial variation of the constitutive and failure response of the FGM is modeled by assigning spatially dependent material properties at each integration point, in an approach similar to that used by Santare and Lambros (2000) to model the behavior of nonhomogeneous materials.

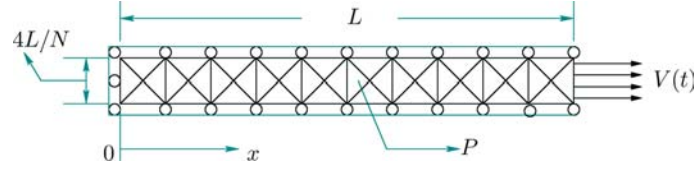


Figure 2. Schematic of the mesh used in the wave propagation study. P is the location where the stresses are computed and N is the number of elements.

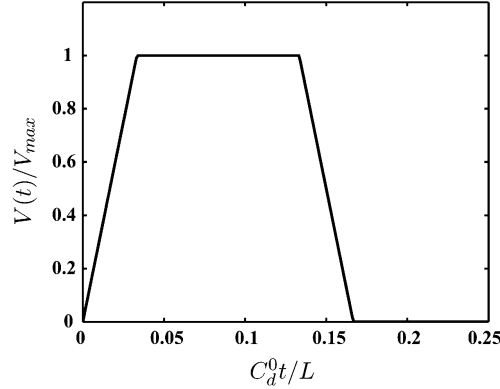


Figure 3. Applied velocity history for 1-D wave propagation problem shown in Figure 2.

3. Wave propagation in FGMs

The accurate capture of wave propagation in the FGM specimen is critical in the numerical modeling of dynamic fracture. In this preliminary section, we perform a detailed analysis to assess the precision of the FE scheme in FGM elastodynamics. In FGMs characterized by a continuous variation of material properties, there are no distinct interfaces that might cause impedance mismatch and lead to wave reflection. However, the numerical implementation relies on the discretization of the domain into finite elements (chosen as 3-node constant strain triangles, or CSTs, in this work) and on the assignment of material properties at the integration point (located at the center of the element). This choice might lead to the artificial introduction of impedance mismatch across element boundaries and thereby to numerical error.

To assess the precision of the FE scheme to capture elastodynamics in FGMs, we investigate the 1-D problem presented in Figure 2. The time-dependent applied velocity $V(t)$ follows the trapezoidal pulse shown in Figure 3, with ramp rise time (Δt_r), dwell time (Δt_d), and unloading time (Δt_u), chosen as $L/30C_d^0$, $L/10C_d^0$, $L/30C_d^0$, respectively, where C_d^0 represents the dilatational wave speed of the material at $x=0$.

Two material variations have been considered in this study. The first one has the following variation for the Young's modulus E_x and mass density ρ_x :

$$E_x = E_0 \left(1 + \beta \frac{x}{L}\right), \quad \rho_x = \rho_0 \left(1 + \beta \frac{x}{L}\right)^{-1},$$

which leads to a linear variation of the dilatational wave speed (C_d^x)

$$C_d^x = \sqrt{\left(\frac{E_0}{\rho_0} \frac{(1-\nu)}{(1-2\nu)(1+\nu)}\right)} \left(1 + \beta \frac{x}{L}\right),$$

and a constant acoustic impedance ($\rho_x C_d^x$). The second material is given by

$$E_x = E_0 \left(1 + \beta \frac{x}{L}\right)^2, \quad \rho_x = \rho_0,$$

and leads to a linear spatial variation of dilatational wave speed and acoustic impedance. In both cases, the Poisson's ratio (ν) is assumed to be constant and the grading parameter β is chosen strictly greater than -1 .

The time step size used in the simulations is limited by the Courant condition

$$\Delta t \leq \Delta t_c = \min_{0 \leq x \leq L} \left(\frac{h_x}{C_d^x}\right), \quad (2)$$

where h_x denotes the element size at location x and is a constant in this wave propagation study (Figure 2). Typically a value of $\Delta t = 0.1 \Delta t_c$ is used in these simulations to ensure time convergence.

The evolution of the σ_{xx} stress component at a point P located near the center of the domain (Figure 2) is presented in Figures 4(a–d) for various values of the material gradient parameter β . The solid and dashed curves, respectively, correspond to the numerical and analytical solutions, and labels 1 and 2 denote the cases associated with constant and linearly varying impedance, respectively. The loading level used in the simulations is chosen small enough to keep the strains at infinitesimal values and thus allow for comparison with the linear elastodynamic analytical solution described in the Appendix A. All curves show the arrival and unloading waves associated with the transient applied velocity $V(t)$. The numerical curves shown in Figure 4(a–c) have been obtained with the same spatial discretization ($h/L = 0.01$). As β decreases and becomes negative, the numerical scheme becomes more dispersive and the numerical solution increasingly deviates from the exact one. As shown in Figure 4(d), further mesh refinement (to $h/L = 0.001$) reduces the numerical error for $\beta = -0.8$.

As apparent in Figure 4, the ability of the finite element scheme to capture the loading and unloading ramp is associated with the amplitude and sign of the material gradient. The results also show that the numerical error is similar for constant and spatially varying impedance cases. These facts are further illustrated in Figure 5, which shows how the relative error on the σ_{xx} stress component at point P depends on the mesh size h and the material gradient parameter β . The error ϵ is defined as

$$\epsilon = \frac{\int_{t_s}^{t_e} |\sigma_{xx}^{\text{numerical}}(x_p, t) - \sigma_{xx}^{\text{analytical}}(x_p, t)| dt}{\int_{t_s}^{t_e} |\sigma_{xx}^{\text{analytical}}(x_p, t)| dt},$$

where t_s and t_e , respectively, denote the time of arrival and departure of the applied velocity pulse at the point of observation P (located at $x = x_p$) and are given by

$$t_s = \frac{L}{\beta C_d^0} \ln \left(\frac{1 + \beta}{1 + \beta x_p / L} \right), \quad t_e = t_s + \frac{L}{6 C_d^0}.$$

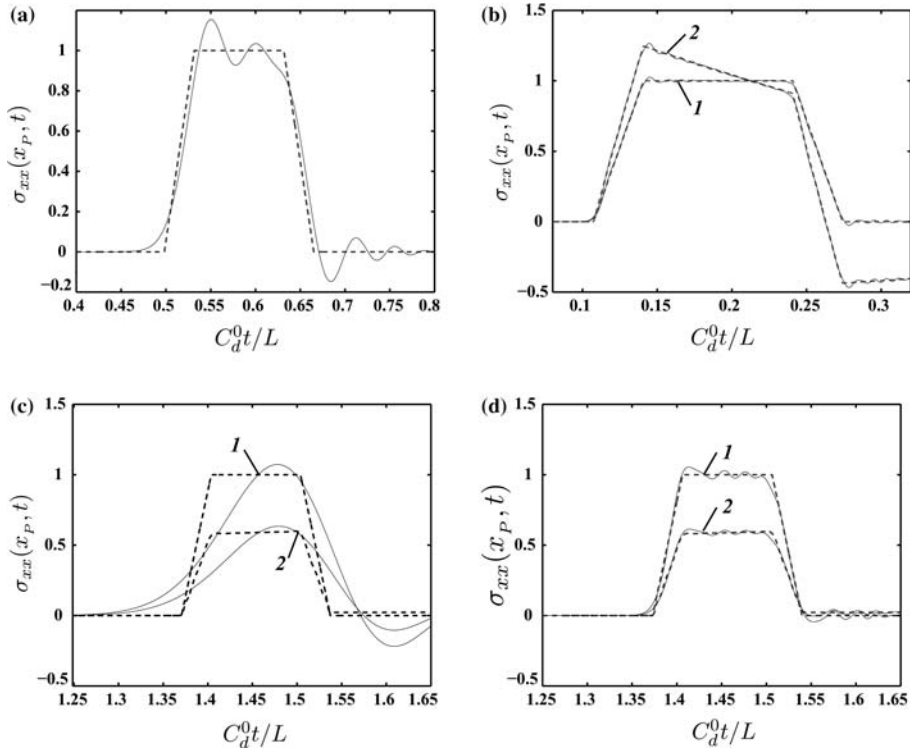


Figure 4. Comparison between the analytical (dashed curves) and numerical (solid curves) evolution of the normalized stress σ_{xx} at a location P near the center of the domain. The curves in Figures (a–c) have been obtained with the coarser mesh with $h/L=0.01$ and with three values of β : $\beta=0$ (a), $\beta=5$ (b) and $\beta=-0.8$ (c). The labels 1 and 2 represent the cases with constant and linearly varying impedance, respectively. (d) corresponds to the finer mesh with $h/L=0.001$ and $\beta=-0.8$. In all subplots, σ_{xx} is normalized with the value of $\rho_P C_d^P V_{\max}$.

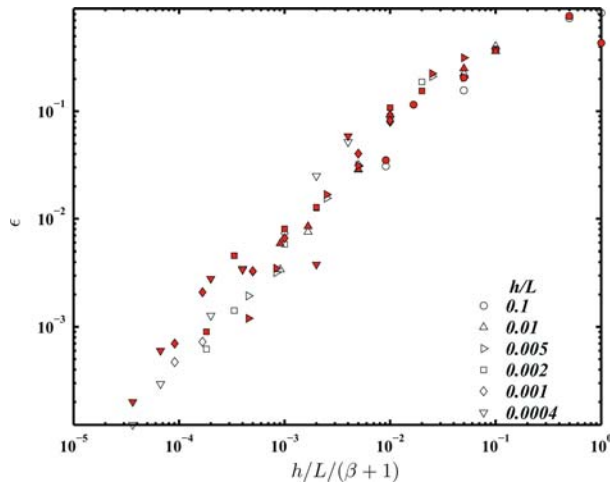


Figure 5. Log-Log plot of the error ϵ vs. $h/L/(\beta+1)$ obtained from the 1-D wave propagation study. The open and filled symbols respectively correspond to the FGM problems with constant and spatially varying impedance.

The open symbols correspond to the various FGM problems with constant impedance, while the filled symbols denote the spatially varying impedance cases. The different shapes represent the various spatial discretizations used in this 1-D wave propagation convergence study. As shown in Figure 5, when plotted in terms of $h/L/(\beta + 1)$, all error curves collapse on the same ‘master curve’, which thereby allows us to quantify readily the effect of the material gradient parameter β on the precision of the elastodynamic FE scheme. Note once again that the convergence trend for the spatially varying impedance problems is very similar to that obtained for the constant impedance cases.

The results in Figure 5 allow us to determine the discretization needed to capture adequately the elastodynamic solution in the FGM sample. This mesh requirement comes in addition to the discretization needed to capture the fracture process itself, i.e., the ability of the finite element solution to simulate the cohesive failure process taking place in the vicinity of the advancing crack front, as discussed in the next section.

4. Simulation of dynamic fracture in model polyester-based FGMs

We now turn our attention to the simulation of the mode I dynamic fracture experiments performed by Parameswaran and Shukla (1998) on model polyester-based FGMs, and used here to validate the numerical scheme described in Section 2. The geometry of the modified compact tension (MCT) specimens used in that experimental study is schematically shown in Figure 6. Spatially varying material properties were obtained by varying the relative content of plasticizer in the polyester resin. In the geometry analyzed in the present validation study, four strips with different plasticizer contents were used, yielding a piecewise continuous variation of the composition from 0% plasticizer content in the region containing the pre-existing crack to

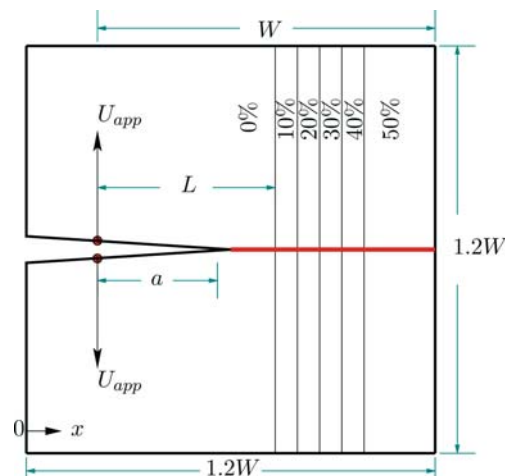


Figure 6. Schematic of the MCT specimen geometry used in the dynamic fracture experiments and simulations. The graded region starts at a distance L from the loading points in steps of 10% plasticizer (beginning with 0%), with the width of the each FGM layer equal to 13 mm ($a = 76$ mm, $W = 200$ mm, $L = 0.5 W$).

Table 1. Quasi-static material properties of polyester-plasticizer strips.

% Plasticizer	Young's modulus E_s (GPa)	Poisson's ratio ν_s	Fracture toughness $K_{Ic,s}$ (MPa $\sqrt{\text{m}}$)
0	3.98	0.32	0.51
10	3.79	0.33	0.55
20	3.51	0.34	0.68
30	3.14	0.35	0.65
40	2.87	0.38	0.67
50	2.20	0.42	0.80

Table 2. Dynamic properties of polyester-plasticizer strips.

Young's modulus, E_{dyn} (GPa)	4.5
Poisson's ratio, ν_{dyn}	0.32
Mass density, ρ (kg/m ³)	1180

50% plasticizer content on the right side of the specimen, with 10% steps in plasticizer content.

The constitutive and failure properties of the various strips are provided by the authors of the experimental study and are summarized in Table 1 for the quasi-static case and Table 2 for the dynamic case. Parameswaran and Shukla have performed the analysis of the experimental results within a linear elastic framework. This assumption is confirmed by the very small strain level (less than 0.2%) obtained in our simulations. As expected, the quasi-static fracture toughness ($K_{Ic,s}$) increases with the plasticizer content, while the quasi-static stiffness (E_s) shows the opposite trend. Interestingly, the dynamic stiffness (E_{dyn}) is substantially higher than its quasi-static counterpart but does not appear to depend on the plasticizer content. The first parameter entering the cohesive failure model, the dynamic fracture toughness ($G_{Ic,\text{dyn}}$) is also rate-dependent and can be described by

$$G_{Ic,\text{dyn}} = \frac{K_{Id}^2}{E_{\text{dyn}}} = \frac{\gamma(v)K_{Ic,s}^2}{E_{\text{dyn}}}, \quad (3)$$

where $\gamma(v)$ quantifies the rate dependence of the fracture toughness, i.e., the dependence of the dynamic fracture toughness (K_{Id}) on the crack velocity (v). This dependence is obtained experimentally and, for the system of interest, we use the data of the experiments performed by Evora et al. (2004) on similar pure polyester MCT specimens. Since these K_{Id} vs. v curves have not been reported for the polyester-plasticizer system, we assume in the present study that its dynamic fracture toughness shows the same rate dependence as the pure polyester material. The second cohesive failure parameter σ_{max} used in the bilinear cohesive model described in Section 2 will be determined in this section.

To simulate the dynamic fracture of the MCT specimen shown in Figure 6, a plane stress CVFE scheme was used with the spatial discretization described in Figure 7. A total of 254 cohesive elements were placed in the path of the mode I

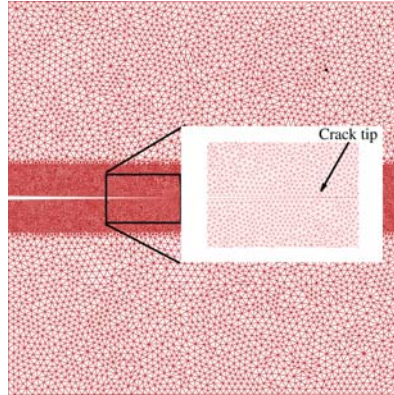


Figure 7. Finite element mesh used in the validation study with the inset showing a close view of the initial crack tip.

crack to accurately capture the failure process in the vicinity of the advancing crack tip. This discretization was adopted following a detailed convergence analysis of the CVFE simulation, with at least five cohesive elements failing in the cohesive zone at all times during the dynamic fracture event.

The specimen was loaded quasi-statically by a pair of point loads applied at a distance a behind the crack tip, which, in the experiments, was intentionally blunted to allow the accumulation of a sufficient amount of strain energy in the specimen prior to crack motion. To capture the initial pre-stressed state of the fracture specimen, a quasi-static stress analysis of the MCT specimen was performed by incrementally applying the applied load up to its experimentally measured critical value. The accumulation of elastic energy associated with the blunting of the pre-crack was modeled by preventing the failure of the cohesive elements by increasing the fracture toughness of the FGM by six orders of magnitude. In this preliminary analysis, we adopted the quasi-static constitutive properties of the material described in Table 1. The resulting displacement and stress state was then introduced as initial conditions in the explicit dynamic CVFE scheme. Two loading conditions were used in the experimental study: in the first one (referred to as Case I), the initial strain energy in the specimen was measured by Parameswaran and Shukla as 0.32 J. They also measured an average crack velocity of 300 m/s in the first experiment. Using this value of crack velocity and the experimental measurements of K_{I_d} vs. v curve obtained by Evora et al. (2004), we extracted the dynamic parameter γ entering Equation (3) to be 1.38. Having determined $G_{I_c, \text{dyn}}$ from Equation (3) in this fashion, we use this first loading case to calibrate the second cohesive failure parameter σ_{max} (or Δ_{nc}) by closely matching the crack advance history. The extracted value is then used in a *fully predictive fashion* in the second loading case (referred to as Case II), which has a lower value of the initial strain energy (0.14 J) and a dynamic parameter γ of 1.16 for an average crack velocity of 260 m/s.

To reduce the size of the parametric space, we considered two scenarios: spatially varying Δ_{nc} with constant σ_{max} and spatially varying σ_{max} with constant Δ_{nc} . In the first scenario, the assumed constant σ_{max} is chosen as a constant fraction of dynamic stiffness and the spatial dependence of the other cohesive parameter Δ_{nc} is obtained

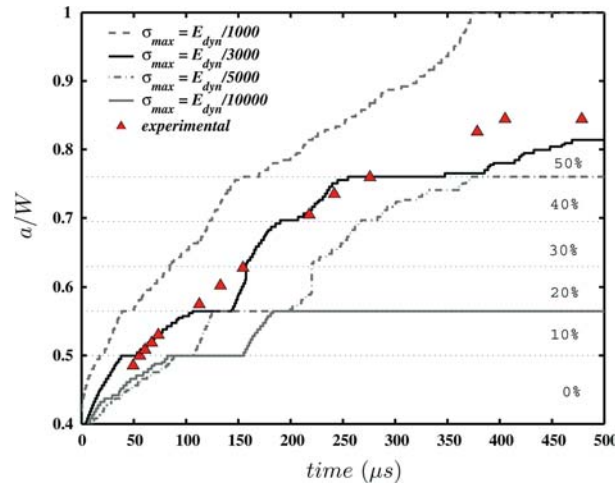


Figure 8. Evolution of the crack tip location curves for Case I: comparison between experimental data (symbols) and numerical results (curves) obtained for different values of σ_{max} . The dotted lines denote the location of the FGM layers.

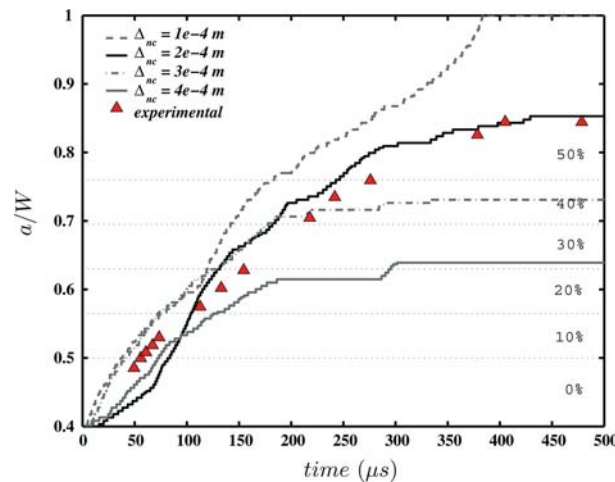


Figure 9. Evolution of the crack tip location curves for Case I: comparison between experimental data (symbols) and numerical results (curves) obtained for different values of Δ_{nc} . The dotted lines denote the location of the FGM layers.

using Equations (1) and (3). The evolution of the crack tip location history (with the origin of the time axis corresponding to the crack initiation time) obtained for four different values of σ_{max} are compared to the experimental data in Figure 8. As shown there, the crack propagation response highly depends on the choice of σ_{max} and is marked with multiple temporary crack arrests at interlayer interfaces, which is contrary to the observed steady crack growth response in the experiments of Parameswaran and Shukla (1998). Therefore, these results are deemed unsatisfactory.

The results of the other approach, i.e., of assuming a constant critical separation Δ_{nc} and allowing for the spatial variation of σ_{max} are presented in Figure 9. Where, the evolution of the crack tip location history obtained for four different values of

Table 3. Cohesive parameters used in Case II simulations, with the superscripts 'I' and 'II' denoting quantities associated with Cases I and II, respectively.

	σ_{\max}^{II}	Δ_{nc}^{II}
Set1	$\alpha^2 \sigma_{\max}^I$	Δ_{nc}^I
Set2	$\alpha \sigma_{\max}^I$	$\alpha \Delta_{nc}^I$
Set3	σ_{\max}^I	$\alpha^2 \Delta_{nc}^I$

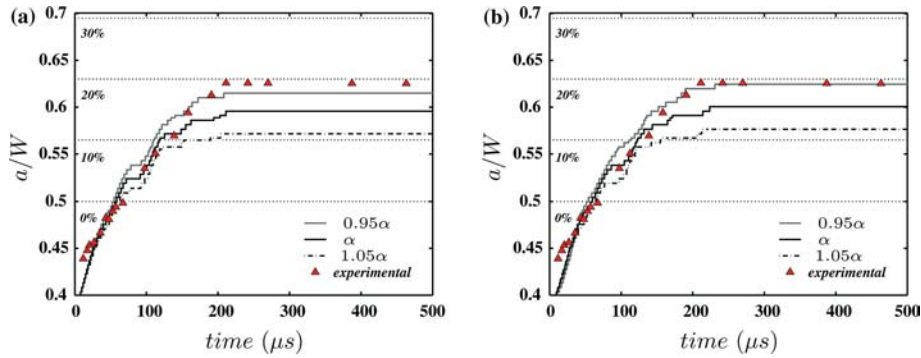


Figure 10. Comparison between predicted and observed time evolutions of the crack tip location a obtained for Case II with $\Delta_{nc} = 200 \mu\text{m}$: (a) Set 1, (b) Set 2.

Δ_{nc} (100, 200, 300 and 400 μm) are compared to the experimental data. As shown there, the crack accelerates rapidly in the more brittle 0% plasticizer layer, progressively slows down and eventually arrests as it encounters increasingly tougher layers. As evident in Figure 9, the crack propagation is quite sensitive to the choice of Δ_{nc} , with higher values of Δ_{nc} leading to crack arrest within the 10–20% plasticizer region, whereas lower values yielding a complete decohesion of the uncracked ligament. The solution obtained with $\Delta_{nc} = 200 \mu\text{m}$ (solid black curve) matches relatively well the experimentally observed crack propagation and arrest behaviors. This leads us to conclude that this approach is more accurate than the scenario used in Figure 8 and is therefore adopted in the validation study of Case II.

Let us rewrite the dynamic fracture toughness of $G_{Ic,dyn}$ for Case II in terms of its Case I counterpart as

$$G_{Ic,dyn}^{\text{Case II}} = \alpha^2 G_{Ic,dyn}^{\text{Case I}}, \quad (4)$$

where α^2 is the ratio of dynamic parameters γ corresponding to the two loading cases and takes the value of 0.84. While the rate dependence of the material toughness is quite clear, the rate dependence of the corresponding cohesive parameters is not as well understood. This suggests the need to simulate the second loading case using three different scenarios (referred to as Sets 1 to 3 in Table 3) obtained by associating the change in fracture toughness to either σ_{\max} or Δ_{nc} or both.

Figures 10(a) and (b), respectively, present the predicted crack propagation curves obtained for Sets 1 and 2, with, in both cases, the experimental data shown using symbols. To account for the experimental scatter associated primarily with the

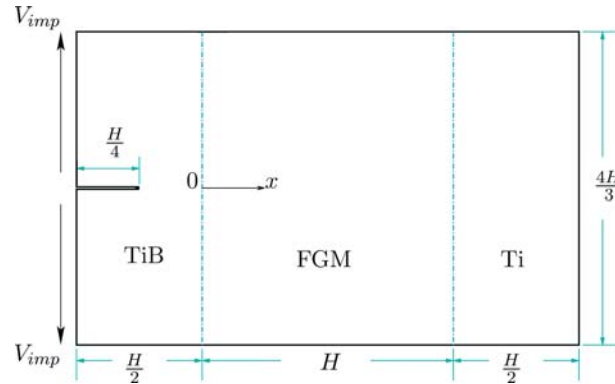


Figure 11. Details of the specimen used in the parametric study with material variation belonging to Case I.

measured values of the dynamic fracture toughness and to quantify the sensitivity of the results on the value of α , we also performed simulations with a $\pm 5\%$ change in the α values and thereby predict the lower and upper bounds of the crack advancement history. Each figure therefore contains three curves, with the solid one corresponding to the reference value of α . For both sets of cohesive parameters, the numerical predictions match the experimental observations quite closely with regards to both the propagation and arrest behaviors. The similarity between the results associated with the three sets of cohesive parameters listed in Table 3 indicates that the crack propagation behavior is clearly dominated by the fracture toughness $G_{Ic,dyn}$ and that, within the range of values considered in Sets 1 to 3, the cohesive parameters only influence weakly the crack propagation response.

5. Parametric study of dynamic fracture of a Ti/TiB FGM

After demonstrating the ability of the CVFE scheme to capture the dynamic failure of FGMs, we now turn our attention to the simulation of dynamic mode I fracture in a metal–ceramic FGM system, and, in particular the Ti/TiB system that is being considered in armor applications (Gooch et al., 1999).

The fracture specimen modeled in this parametric study is shown in Figure 11. It contains a mathematically sharp edge crack of length $H/4$, where $H = 12$ mm is the width of the FGM layer. In most of the simulations presented hereafter (referred to in this section as Case I), the pre-crack is introduced in the TiB layer and the crack therefore propagates from the more brittle ceramic component to the more tough metallic one. However, we also consider at the end of the study the reverse case (referred to as Case II) where the crack starts from the metallic side and propagates toward the ceramic layer. The specimen is assumed to be thin and plane stress conditions are thus adopted. Figure 11 also illustrates the coordinate frame used in this study, centered on the fracture plane at the beginning of the FGM region. As also shown in Figure 11, the specimen is wedge-loaded in mode I along its left edge while the other edges are traction free. In all the simulations presented in this section, the applied velocity V_{imp} is ramped up linearly during the first 167 ns up to a value of 10 m/s and is then maintained constant for the remainder of the fracture event.

Table 4. Material properties of Ti/TiB FGM used in the parametric study.

	Ti	TiB
<i>Volumetric</i>		
Young's modulus, E (GPa)	107	375
Poisson's ratio, ν	0.34	0.14
Mass density, ρ (kg/m ³)	4500	4710
<i>Cohesive</i>		
Fracture toughness, G_{Ic} (kJ/m ²)	150	0.11
σ_{\max} (MPa)	620	4

The finite element discretization of the fracture specimen is similar to that used in the validation study presented in Section 4 and involves approximately 245 cohesive elements with an average length of $85\ \mu\text{m}$ placed along the fracture plane ahead of the pre-crack. The time step size adopted in this study is 1 ns.

The constitutive and failure properties for Ti and TiB have been taken from Jin et al. (2002) and are summarized in Table 4. Note the three-order magnitude difference between the fracture toughness of the metallic and ceramic components. As shown below, this difference will play a key role in the fracture response of the FGM system. In all the simulations presented in this section, the strain level remains below 0.5%. For the FGM region, in absence of reliable experimental measurements, we assume a power-law variation of the constitutive and failure properties following the relation

$$\frac{\lambda_x - \lambda_{x_1}}{\lambda_{x_2} - \lambda_{x_1}} = \left(\frac{x - x_1}{x_2 - x_1} \right)^n, \quad (5)$$

where λ_x denotes any constitutive (Young's modulus E , Poisson's ratio ν and density ρ) or failure (tensile strength σ_{\max} and fracture toughness G_{Ic}) property at location x with x_1 and x_2 , respectively, representing the start and end locations of the FGM region ($x_1 = 0$ and $x_2 = H$ in this case). As illustrated in Figure 12, the exponent n entering Equation (5) determines the sharpness of the material transition, with small and large values of n generating a bias toward the first and second materials, respectively, while the limiting cases ($n = 0$ and $n = \infty$) correspond to sharp interfaces between the two components.

The evolution of the crack tip location (shifted such that a value of zero corresponds to the crack arrival at the FGM region) is shown in Figure 13 for the pure ceramic and pure metal cases and for five FGM cases with values of the exponent n equal to 0.1, 0.5, 1, 2 and 10.

The wave speed used to normalize the time axis is the Rayleigh wave speed in the ceramic component (C_R^c). The crack tip is defined as the right-most cohesive integration point along the fracture plane for which the damage parameter \mathcal{S} introduced in Section 2 reaches zero. As expected, since the crack initiates in the ceramic layer, the initial phase of the fracture event in the FGM case is the same as for the homogeneous TiB specimen, and the crack quickly accelerates to reach quasi-steady-state as it enters the graded region. At that point, however, due to the substantial difference

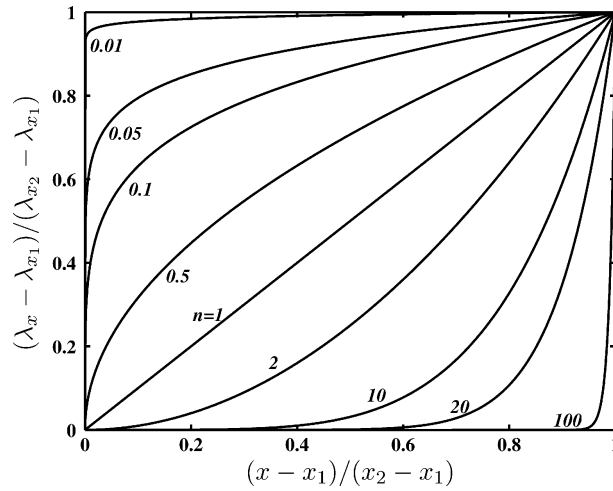


Figure 12. Effect of exponent n on the variation of the material properties λ_x described by Equation (5).

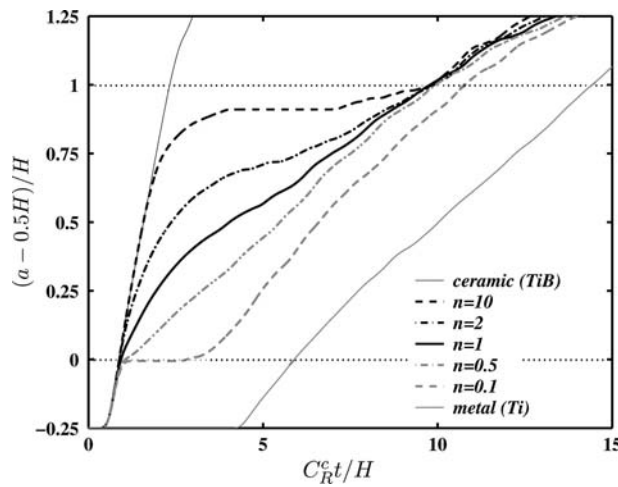


Figure 13. Evolution of the crack tip location for the ceramic-to-metal crack propagation problem for the FGM with five values of the exponent n , and for the pure ceramic (TiB) and pure metal (Ti) cases. The dotted horizontal lines correspond to the start and end of the graded region in the FGMs.

in fracture resistance between TiB and Ti, the evolution of the crack length starts to differ greatly from the pure ceramic case. The crack then slows down to approach the lower crack speed characteristic of the pure Ti case. The transition strongly depends on the exponent n : for small values of n , the sharp transition to high fracture toughness leads to a temporary arrest of the crack, the duration of which increases with decreasing values of n . For high values of n , the crack also experiences arrest in the FGM region before restarting its propagation in the tougher predominantly Ti region. No crack arrest is observed for intermediate values of n ($n=2, 1$ and 0.5) and a smooth transition is observed in the crack propagation speed from the fast behavior associated with TiB to the slower fracture response associated with Ti.

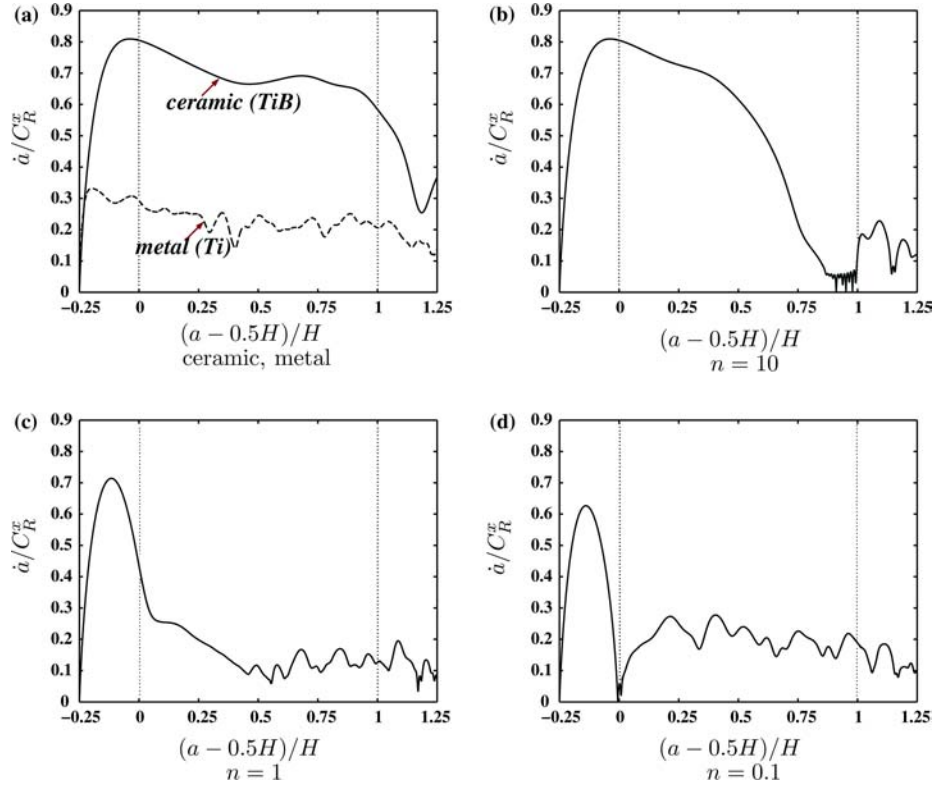


Figure 14. Crack velocity vs. crack advance curves obtained for the ceramic-to-metal fracture problem: (a) reference homogeneous ceramic and metallic cases; (b–d) three representative values of the property gradient exponent n : $n=10$ (b), $n=1$ (c) and $n=0.1$ (d). The crack velocity is normalized by the local value of the Rayleigh wave speed C_R^x . The vertical dotted lines correspond to the limits of the FGM region.

The evolution of the crack propagation speed is also presented in Figure 14 as a function of the crack advance for the homogeneous ceramic and metallic cases (Figure 14a) and for three values of the property gradient exponent n : $n=10$ (Figure 14b), $n=1$ (Figure 14c) and $n=0.1$ (Figure 14d). The crack speed is normalized by the local value of the Rayleigh wave speed (C_R^x).

As shown in Figure 14(a), the two limiting (homogeneous ceramic and metallic) cases yield two very different crack propagation speeds: about 60% of the TiB Rayleigh wave speed in the pure ceramic case and about 25% of the Ti Rayleigh wave speed in the pure metallic case. When the material gradient is biased toward the Ti region (i.e., for $n=10$), the crack propagation behavior in the first half of the FGM layer is almost identical to the pure TiB case. In the remainder of the FGM layer, the sharp transition to more fracture resistant properties lead to a drastic slowdown and even arrest of the crack before it eventually enters the Ti region. In the ‘linear FGM case’ ($n=1$), the crack slow down is much more progressive and no arrest is detected. Finally, in the last FGM case ($n=0.1$), the crack is arrested as soon as it enters the FGM region, before reinitiating its motion and reaching propagation speeds similar to the homogeneous Ti case (i.e., about 25% of the corresponding Rayleigh wave speed).

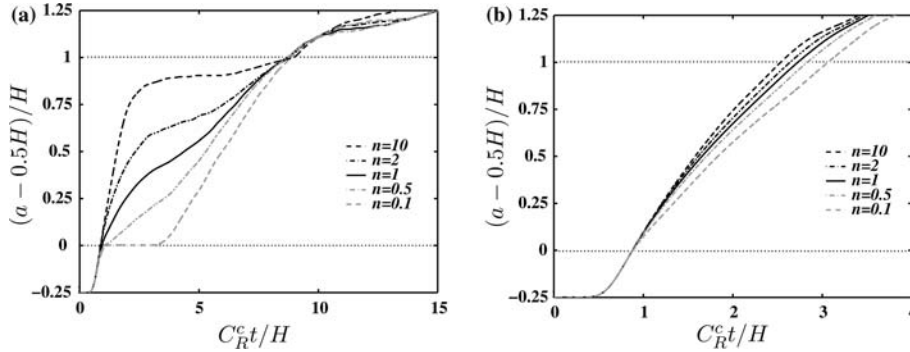


Figure 15. Relative effect of the gradient in constitutive and failure properties on the ceramic-to-metal fracture event: evolution of the crack length a for constant constitutive properties but varying failure properties (a) and for constant failure properties but varying constitutive properties (b). In both cases, results are shown for representative values of the gradient exponent n and the constant properties are chosen as those of TiB.

It should be noted once again that, in the results presented so far, all material properties are assumed to follow the same spatial variation described by Equation (5). It might therefore be of interest to differentiate the relative role of the material gradient in constitutive and failure properties on the dynamic fracture response. This study is summarized in Figure 15, which presents the time evolution of the crack length for constant constitutive properties (chosen as those of TiB) and varying failure properties (Figure 15a), and for constant failure properties (chosen as those of TiB) and varying constitutive properties (Figure 15b). As apparent there, the gradation in failure properties affect the fracture response of the FGM specimen much more than the spatial variation of the constitutive properties. This is to be expected considering the substantial mismatch in failure strength and fracture toughness between the TiB and Ti constituents. A similar conclusion is reached if the constant properties are chosen as those of Ti.

To conclude this parametric study of dynamic fracture in a Ti/TiB FGM specimen, we investigate the reverse problem (Case II) where the crack initiates in the metallic (Ti) zone and propagates dynamically through the FGM region toward the ceramic (TiB) zone. The evolution of the crack length (shifted in a manner similar to Figure 13) is presented in Figure 16 for three representative values of the material gradient exponent n and for the two reference homogeneous cases.

As apparent in this figure, the dynamic failure response in Case II is very different from Case I. While a continuous crack motion with, in some cases, crack arrest, was observed in the curves presented in Figure 13, the FGM simulations associated with Case II are characterized by a sudden jump of the crack length (denoted by vertical segments in Figure 16). This discontinuous crack motion can be explained once again by the large mismatch between the failure properties of Ti and TiB, which strongly affects the time and location of the onset of failure in the specimen. This fact is illustrated in Figure 17, which presents snapshots of the spatial distribution of the crack opening displacement normalized by the local value of its critical value for $n=0.1$ (Figure 17a) and $n=10$ (Figure 17b). As in previous figures, the vertical dotted lines correspond to the bounds of the FGM region, while the horizontal line

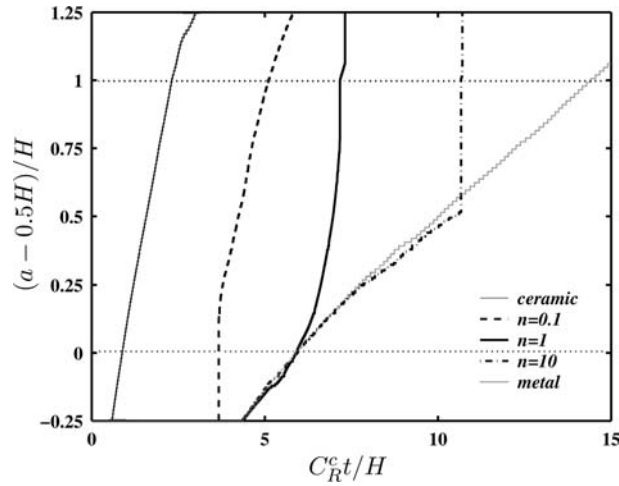


Figure 16. Evolution of the crack length for the metal-to-ceramic crack propagation problem (Case II), for three values of the exponent n and for the two reference homogeneous (ceramic and metallic) cases. The horizontal dotted lines denote the bounds of the FGM region.

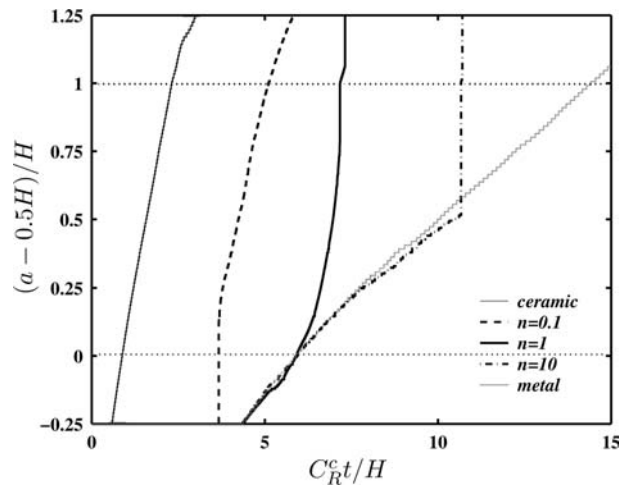


Figure 17. Evolution of the spatial distribution of the crack opening displacement normalized by its local critical value obtained in the metal-to-ceramic fracture problem: (a) $n=0.1$, time from $8.1 \mu\text{s}$ (1) to $10.1 \mu\text{s}$ (5) with $0.5 \mu\text{s}$ time interval; (b) $n=10$ with time from $23.6 \mu\text{s}$ (1) to $27.6 \mu\text{s}$ (5) with $1 \mu\text{s}$ time interval.

denotes the critical value of the displacement jump beyond which complete failure is achieved (i.e., the location of the crack tip(s)).

In the case $n=0.1$, for which a sharp transition exists between Ti and TiB properties biased toward the beginning of the FGM region, the sharp decline in the critical crack opening displacement value leads to the creation, ahead of the main crack, of a secondary failure region, whose right tip propagates rapidly through the FGM region while the left tip coalesces with the main crack. Based on our aforementioned definition of the crack tip location, the appearance of this secondary crack leads to the vertical segment apparent in Figure 16. In the other limiting case, $n=10$, a similar

discontinuous crack motion is observed, but this time in the vicinity of the end of the FGM region. The sharp drop in failure properties present there leads to the creation of a secondary crack, which propagates ahead of the main crack into the TiB region.

6. Conclusions

A numerical method based on a CVFE scheme has been extended to capture the dynamic crack propagation in FGMs. The effect of the amplitude and sign of the material gradient on the ability of the explicit FE scheme to capture elastodynamic wave propagation has been studied through a detailed convergence analysis of 1-D wave propagation. The FGM CVFE scheme has been validated by simulating dynamic fracture experiments on model polyester-based FGMs performed by Parameswaran and Shukla (1998). The failure properties of the model FGM were extracted through comparison with experimental measurements of crack motion associated with a chosen loading case and then used in a predictive fashion for a different loading case. The scheme has then been used in a parametric study of dynamic mode I crack propagation in Ti/TiB FGM specimens. For that problem, characterized by a large mismatch in fracture properties between the metallic and ceramic components, results showed a great sensitivity of the crack motion to the gradient of the cohesive failure parameters.

Acknowledgements

The authors gratefully acknowledge the National Science Foundation for supporting this research through grant CMS 01-15954. They also wish to thank Prof. A. Shukla and Prof. V. Parameswaran for providing some valuable insight on their experimental data.

Appendix A

The solution for the 1-D wave propagation problem in linear elastic FGMs described in Section 3 is obtained using the Laplace transform following the approach described by Chiu and Erdogan (1999). The wave equation is

$$\frac{\partial \sigma_{xx}}{\partial x} = \frac{\partial}{\partial x} \left(\bar{E}_x \frac{\partial u}{\partial x} \right) = \rho_x \frac{\partial^2 u}{\partial t^2}, \quad (\text{A.1})$$

where $u(x, t)$ is the displacement.

The variation of the properties considered here are

$$\bar{E}_x = \bar{E}_0 \left(1 + \beta \frac{x}{L} \right)^m, \quad \rho_x = \rho_0 \left(1 + \beta \frac{x}{L} \right)^n, \quad (\text{A.2})$$

where m, n, β are arbitrary real constants with $\beta > -1$, \bar{E}_0 and ρ_0 are the effective stiffness and mass density evaluated at $x=0$. The effective stiffness under plane strain conditions is given by

$$\bar{E}_x = \frac{E_x(1-\nu)}{(1+\nu)(1-2\nu)},$$

where E_x is the spatially varying Young's modulus and ν , the assumed constant Poisson's ratio.

Equation (A.1) is solved with quiescent initial conditions:

$$u(x, 0) = 0, \quad \frac{\partial}{\partial t} u(x, 0) = 0, \quad 0 < x < L,$$

and with the imposed velocity boundary condition at $x = L$:

$$\frac{\partial}{\partial t} u(L, t) = V(t).$$

Following the method of Chiu and Erdogan (1999), Equations (A.1) and (A.2) are solved in the Laplace domain as, for $m = n + 2$,

$$\hat{u}\left(\frac{x}{L}, p\right) = \frac{\hat{V}(p)}{p} \left[\frac{(\beta \frac{x}{L} + 1)^{s_1} - (\beta \frac{x}{L} + 1)^{s_2}}{(\beta + 1)^{s_1} - (\beta + 1)^{s_2}} \right],$$

where

$$s_1, s_2 = -\left(\frac{n+1}{2}\right) \pm \sqrt{\frac{(n+1)^2}{4} + \frac{p^2}{\beta^2}}.$$

When $m \neq n + 2$,

$$\hat{u}\left(\frac{x}{L}, p\right) = \frac{\hat{V}(p)}{p} \left(\frac{\beta \frac{x}{L} + 1}{\beta + 1}\right)^{\frac{1-m}{2}} \left[\frac{K_\psi(p_1)I_\psi(p_3) - I_\psi(p_1)K_\psi(p_3)}{K_\psi(p_1)I_\psi(p_2) - I_\psi(p_1)K_\psi(p_2)} \right],$$

where

$$p_1 = \left| \frac{2p}{(n-m+2)\beta} \right|,$$

$$p_2 = \left| \frac{2p}{(n-m+2)\beta} \right| (\beta + 1)^{\frac{n-m+2}{2}},$$

$$p_3 = \left| \frac{2p}{(n-m+2)\beta} \right| \left(\beta \frac{x}{L} + 1\right)^{\frac{n-m+2}{2}},$$

while $I_\psi(z)$ and $K_\psi(z)$ are the modified Bessel functions of the first and second kind with

$$\psi = \left| \frac{1-m}{n-m+2} \right|.$$

The stress σ_{xx} can then be obtained using Equation (A.1).

References

- Abanto-Bueno, J. and Lambros, J. (2002). Investigation of crack growth in functionally graded materials using digital image correlation. *Engineering Fracture Mechanics* **69**, 1695–1711.
- Atkinson, C. and List, R.D. (1978). Steady state crack propagation into media with spatially varying elastic properties. *International Journal of Engineering Science* **16**, 717–730.

- Babaei, R. and Lukasiewicz, S.A. (1998). Dynamic response of a crack in a functionally graded material between two dissimilar half planes under anti-plane shear impact load. *Engineering Fracture Mechanics* **60**, 479–487.
- Banks-Sills, L., Eliasi, R. and Berlin, Y. (2002). Modeling of functionally graded materials in dynamic analyses. *Composites Part B: Engineering* **33**, 7–15.
- Batra, R.C. (1980). Finite plane strain deformations of rubberlike materials. *International Journal of Numerical Methods in Engineering* **15**, 145–156.
- Bi, X., Li, Z., Geubelle, P.H. and Lambros, J. (2002). Dynamic fiber debonding and frictional push-out in model composite systems: numerical simulations. *Mechanics of Materials* **34**, 433–446.
- Butcher, R.J., Rousseau, C.E. and Tippur, H.V. (1999). A functionally graded particulate composite: preparation, measurements and failure analysis. *Acta Materialia* **47**, 259–268.
- Camacho, G.T. and Ortiz, M. (1996). Computational modelling of impact damage in brittle materials. *International Journal of Solids and Structures* **33**, 2899–2938.
- Chalivendra, V.B., Shukla, A., Bose, A. and Parameswaran, V. (2003). Processing and mechanical characterization of lightweight polyurethane composites. *Journal of Materials Science* **38**, 1631–1643.
- Chiu, T.C. and Erdogan, F. (1999). One-dimensional wave propagation in a functionally graded elastic medium. *Journal of Sound and Vibration* **222**, 453–487.
- Choi, H.J. (1996). Bonded dissimilar strips with a crack perpendicular to the functionally graded interface. *International Journal of Solids and Structures* **33**, 4101–4117.
- Eischen, J.W. (1987). Fracture of nonhomogeneous materials. *International Journal of Fracture* **34**, 3–22.
- Erdogan, F. (1995). Fracture mechanics of functionally graded materials. *Composites Engineering* **5**, 753–770.
- Espinosa, H.D., Zavattieri, P.D. and Dwivedi, S. (1998). A finite deformation continuum/discrete model for the description of fragmentation and damage in brittle materials. *Journal of the Mechanics and Physics of Solids* **46**, 1909–1942.
- Evora, V., Jain, N. and Shukla, A. (2004). Static and dynamic fracture toughness and crack propagation in nanocomposites. In: *Proceedings of Society of Experimental Mechanics Annual Summer Conference, Costa Mesa, CA*. article in press.
- Feng, W.J. and Zou, Z.Z. (2003). Dynamic stress field for torsional impact of a penny shaped crack in a transversely isotropic functionally graded strip. *International Journal of Engineering Science* **41**, 1729–1739.
- Geubelle, P.H. and Baylor, J.S. (1998). Impact-induced delamination of composites: a 2D simulation. *Composites Part B: Engineering* **29B**, 589–602.
- Gooch, W.A., Chen, B.H.C., Burkins, M.S., Palicka, R., Rubin, J. and Ravichandran, R. (1999). Development and ballistic testing of a functionally gradient ceramic/metal applique. *Materials Science Forum* **308–311**, 614–621.
- Gu, P. and Asaro, R.J. (1997). Crack deflection in functionally graded materials. *International Journal of Solids and Structures* **34**, 3085–3098.
- Jiang, L.Y. and Wang, X.D. (2002). On the dynamic crack propagation in an interphase with spatially varying elastic properties under inplane loading. *International Journal of Fracture* **114**, 225–244.
- Jin, Z.H. and Batra, R.C. (1996). Some basic fracture mechanics concepts in functionally graded materials. *Journal of the Mechanics and Physics of Solids* **44**, 1221–1235.
- Jin, Z.H. and Noda, N. (1994). Crack-tip singular fields in nonhomogeneous materials. *Transactions of the ASME: Journal of Applied Mechanics* **61**, 738–740.
- Jin, Z.-H., Paulino, G.H. and Dodds, R.H. Jr. (2002). Finite element investigation of quasi-static crack growth in functionally graded materials using a novel cohesive zone fracture model. *Transactions of the ASME: Journal of Applied Mechanics* **69**, 370–379.
- Jin, Z.-H., Paulino, G.H. and Dodds, R.H. Jr. (2003). Cohesive fracture modeling of elastic plastic crack growth in functionally graded materials. *Engineering Fracture Mechanics* **70**, 269–283.
- Kawasaki, A. and Watanabe, R. (1987). Finite element analysis of thermal stress of the metal/ceramic multi-layer composites with compositional gradients. *Journal of Japan Institute of Metals* **51**, 525–529.
- Lambros, J., Santare, M.H., Li, H. and Sapna III, G. (1999). A novel technique for the fabrication of laboratory scale functionally graded materials. *Experimental Mechanics* **39**, 183–189.

- Lee, K.H. (2004). Characteristics of a crack propagating along the gradient in functionally gradient materials. *International Journal of Solids and Structures*. article in press.
- Li, C.Y., Zou, Z.Z. and Duan, Z.P. (1999). Torsional impact of transversely isotropic solid with functionally graded shear moduli and a penny-shaped crack. *Theoretical and Applied Fracture Mechanics* **32**, 157–163.
- Li, H., Lambros, J., Cheeseman, B.A. and Santare, M.H. (2000). Experimental investigation of the quasi-static fracture of functionally graded materials. *International Journal of Solids and Structures* **37**, 3715–3732.
- Maiti, S. and Geubelle, P.H. (2004). Mesoscale modeling of dynamic fracture of ceramic materials. *CMES: Computer Modeling in Engineering & Sciences* **5**, 91–102.
- Meguid, S.A., Wang, X.D. and Jiang, L.Y. (2002). On the dynamic propagation of a finite crack in functionally graded materials. *Engineering Fracture Mechanics* **69**, 1753–1768.
- Parameswaran, V. and Shukla, A. 1998, Dynamic fracture of a functionally gradient material having discrete property variation. *Journal of Materials Science* **33**, 3303–3311.
- Parameswaran, V. and Shukla, A. (1999). Crack-tip stress fields for dynamic fracture in functionally gradient materials. *Mechanics of Materials* **31**, 579–596.
- Parameswaran, V. and Shukla, A. (2002). Near-tip out of plane displacement fields for dynamic crack propagation in functionally graded materials. *Mechanics Research Communications* **29**, 397–405.
- Paulino, G.H. and Kim, J.-H. (2002). Isoparametric graded finite elements for non-homogeneous isotropic and orthotropic materials. *Transactions of the ASME: Journal of Applied Mechanics* **69**, 502–514.
- Rousseau, C.E. and Tippur, H.V. (2001). Dynamic fracture of compositionally graded materials with cracks along the elastic gradient: experiments and analysis. *Mechanics of Materials* **33**, 403–421.
- Santare, M.H. and Lambros, J. (2000). Use of graded finite elements to model the behavior of non-homogeneous materials. *Transactions of the ASME: Journal of Applied Mechanics* **67**, 819–822.
- Santare, M.H., Thamburaj, P. and Gazonas, G.A. (2003). The use of graded finite elements in the study of elastic wave propagation in continuously nonhomogeneous materials. *International Journal of Solids and Structures* **40**, 5621–5634.
- Uemura, S. (2003). The activities of FGM on new application. *Materials Science Forum* **423-425**, 1–10.
- Wang, B.L., Han, J.C. and Du, S.Y. (1999). Functionally graded penny-shaped cracks under dynamic loading. *Theoretical and Applied Fracture Mechanics* **32**, 165–175.
- Wang, Z. and Nakamura, T. (2004). Simulations of crack propagation in elastic-plastic graded materials. *Mechanics of Materials* **36**, 601–622.
- Xu, X.P. and Needleman, A. (1996). Numerical simulations of dynamic crack growth along an interface. *International Journal of Fracture* **74**, 289–324.
- Yue, Z.Q., Xiao, H.T. and Tham, L.G. (2003). Boundary element analysis of crack problems in functionally graded materials. *International Journal of Solids and Structures* **40**, 3273–3291.
- Zhang, C., Savadis, A., Savadis, G. and Zhu, H. (2003). Transient dynamic analysis of a cracked functionally graded material by a BIEM. *Computational Materials Science* **26**, 167–174.